Particle Capture by a Rotating Disk in a Kitchen Exhaust Hood

Shiyu Zhang[a], Sumei Liu[a,b,*] and Qingyan Chen[b]

[a]*Tianjin Key Laboratory of Indoor Air Environmental Quality Control, School of Environmental Science and Engineering, Tianjin University, Tianjin 300072, China*
[b]*School of Mechanical Engineering, Purdue University, West Lafayette, IN 47905, USA*

[*]*Corresponding email: smliu@tju.edu.cn*

HIGHLIGHTS

- Generation of oil droplets in experiment by a realistic method
- CFD simulations of air velocity field and particle trajectories for a rotating disk
- Verification of the computed results with corresponding experimental data
- Improvements of capture efficiency of the rotating disk

ABSTRACT

Chinese cooking produces large numbers of particles that can cause both indoor and outdoor air quality problems. To reduce the extraction of particles to the outdoor air, this investigation studied capture efficiency of a rotating disk in an exhaust hood. The studies were performed experimentally in a wind tunnel and numerically by computational fluid dynamics (CFD) models with the Lagrangian method for tracking particle trajectories. The experimental data was used to identify the best turbulence model among the three tested in the CFD simulations. The results show that the capture efficiency increased with disk rotation speed and particle size but decreased with exhaust airflow rate. The CFD simulations provided detailed information about the mechanisms by which particles of different sizes were captured by the rotating disk. CFD was then used to explore two methods for improving the capture efficiency: adding more wires to the middle and outer zones of the disk, and using two layers of disks. Both methods can increase the capture efficiency of the rotating disk at an acceptable pressure loss.

Keywords: CFD; Experimental measurements; Disk design; Moving grid; Lagrangian method; Inertial force; Pressure drop

1. Introduction

Particles generated during cooking are an important source of indoor and outdoor air pollution. The average number and mass concentration of PM2.5 in Chinese kitchens were found to increase by more than 10 times during cooking in comparison with non-cooking hours (Gao et al. 2013; See and Balasubramanian 2006). Epidemiological results demonstrated a significant link between negative health effects and exposure to particulate matter from cooking (Lu et al. 2019; Metayer et al. 2002; POPE III 2000; Sze-To et al. 2012; Wang et al. 2017). The range hoods used in present Chinese homes and restaurants discharge cooking fumes to the outdoor environment without a disposal process, resulting in severe haze (Zhu et al. 2014). Xiao et al. (2018) investigated contaminant levels at a fume outlet outside a Chinese restaurant and found that the PM2.5 level increased by up to 15.9 times, and the PM10 level by 3.6 times, during cooking. Thus, to reduce outdoor air pollution, it is important to remove particle matter during cooking.

47   To effectively remove particle matter, one should understand the particle emission rate
48 and size. Different cooking styles lead to different particle emission rates (Kang et al. 2019;
49 See and Balasubramanian, 2006; See and Balasubramanian, 2008). Cooking temperature and
50 oil type are the primary factors in particle concentration and size distribution. Particle size
51 increases with cooking temperature, and oil with a higher smoke temperature disperses fewer
52 particles (Torkmahalleh et al. 2012). The particle size can vary from nanometers to tens of
53 microns. Previous studies focused mainly on the number concentration of ultrafine particles (
54 <0.1 μm) or PM 2.5 because they contribute to more than 90% of the number concentration
55 (Li et al. 1993). However, when the particle size is small, a high number concentration does not
56 contribute greatly to the particle mass. On the other hand, a small number of larger particles
57 can account for a high proportion of the particle mass (Welch and Kuehn 2003). However,
58 particles with a diameter larger than 18 μm are too heavy to remain airborne and can easily
59 drop out of the airstream (ASHRAE Standard 62.1 2007). Thus, one should study particles with
60 diameters between 2.5 and 18 μm for their impact on outdoor air pollution.
61   A range hood is typically employed to remove particulate matter from a kitchen. The hood
62 performance depends on the filtering technology used, the exhaust airflow rate, aerodynamic
63 design, conditions in the indoor space, etc. (Lunden et al. 2015; Rim et al. 2012; Singer et al.
64 2012). Capture efficiency (CE) is a frequent criterion for hood performance (Delp and Singer
65 2012). The most important part of a hood is its grease-removal system, which reduces the
66 volume of grease in the exhaust airstream. The system may use a static steel mesh filter, a baffle
67 filter, a cyclonic filter, or a rotating filter (Rajendran and Otzen 1990). The static mesh filter is
68 used in the majority of hoods on the market. Grease particles impinge upon and are collected
69 by the filter, while interstices permit clean air to pass through. The filter requires frequent
70 maintenance to prevent clogging by particles entrained in the airstream. The baffle filter
71 consists of a series of overlapping baffles that force the grease-laden exhaust air to change
72 direction several times within the filter. The grease is removed from the air stream by
73 centrifugal force. However, the baffle system has a very high pressure drop (Alexander and
74 Salpietra 2012; Kwok and Robison 2011). The cyclonic filter also separates unwanted grease
75 by centrifugal force. Fumes are typically injected tangentially into the cyclonic separator to
76 form a circular flow. The centrifugal forces act on particles and force them toward the perimeter
77 of the separation chamber where the grease is collected (Antoun 1999; Huber 2005). The
78 efficiency of the mesh and baffle filters is lower than 10% when the particle size is smaller than
79 3 micron and 25% for 10 micron particles. The efficiency of the cyclonic filter can be 85% for
80 10 micron particles. However, all the above filters require repeated cleaning to avoid clogging.
81 A rotating filter, meanwhile, can theoretically improve the efficiency with enhanced centrifugal
82 force, since the rotating part increases the probability of collision between particles and filter
83 media. The particles that collect on the filter accumulate to form large droplets and can be easily
84 removed; thus, the filter has a self-cleaning ability.
85   There are two different rotating filters on the market: one with a fine net filter that has a
86 bore diameter of less than 2 mm, and the other with radially twined wires. Li et al. (2017)
87 observed a high capture efficiency with the fine net filter when the rotating speed was high and
88 the rotating mesh filter was dense. This device could create a very high pressure drop, although
89 little information is available. Meanwhile, for filters with rotating radially twined wires, very
90 few studies have been published. Because of the wires are placed sparsely, the capture
91 efficiency with the rotating radially twined wires may not be very high, but the pressure drop
92 would be low as well. Sun (2009) found that the capture efficiency for 8 micron particles by a
93 hood with this type of filter was only 20%. Therefore, a hood with rotating radially twined wires
94 (hereafter a hood with a rotating filter disk) should be studied with the goal of improving its
95 efficiency.

The objective of this investigation was to study the capture mechanism of a hood with a rotating filter disk. In this paper we will examine various parameters that could significantly affect the capture efficiency and pressure drop.

2. Methods

Our study focused on a range hood with a rotating filter disk. The rotating disk was a component of the purification module, which also included a deflector and a motor as shown in Fig. 1. The deflector was used to induce the airflow, and the motor rotated the disk. The rotating disk consisted of two layers of fine metal wires twined radially. The disk used for the present study consisted of 160 wires per layer and eight supporting bars between the two layers. When the disk rotated at a high speed, particles in the air stream from the cooking fumes would collide with and be captured by the wires. Because of the high rotation speed, the centrifugal force would move the captured particles or grease to the outer ends of the wires. The grease could then be collected along the perimeter of the supporting frame and removed easily without frequent maintenance.
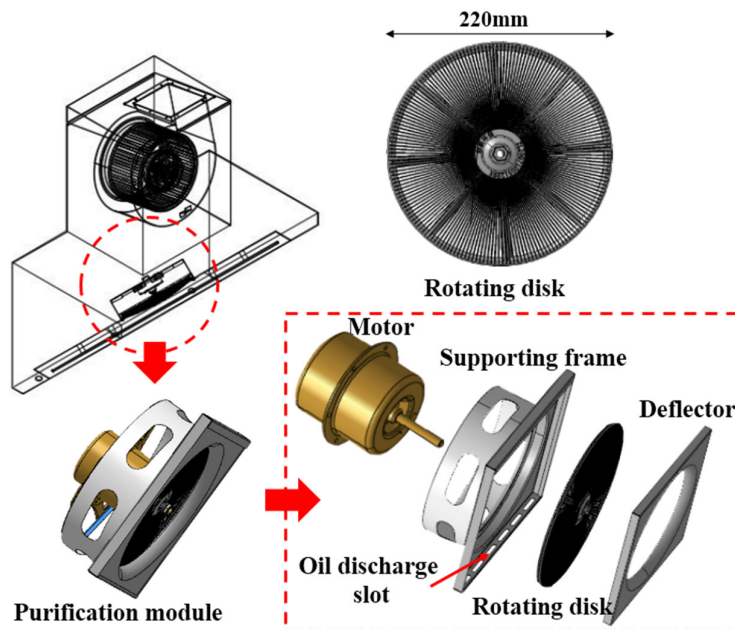

Fig. 1. The purification module in a kitchen exhaust hood

The study of capture efficiency by a hood can be conducted through numerical simulations by computational fluid dynamics (CFD) or experimental measurements in a laboratory. The experimental measurements are reliable, but they are expensive and time consuming, since it is not easy to change the hood structure. Meanwhile, the CFD simulations can produce informative results, but the model used may not be reliable. Thus, the optimal approach is to conduct limited experimental measurements to obtain data for validating the CFD model, and to use the CFD model for further analysis of the performance of the rotating disk.

2.1 Experimental setup

Our experiment was conducted in a large laboratory with dimensions of 10 m × 8 m × 5 m and stable thermo-fluid conditions. The room air temperature was controlled at 23±1°C and relative humidity at 42±2%. Ventilation conditions were stable during the experiments (doors

128   and windows were closed, and the mechanical ventilation through two vents on the ceiling was
129   operational). Fig. 2 (a) shows a 4.8 m-long wind tunnel test rig that was used for the present
130   study; it was placed in the center of the laboratory. The upstream and downstream sections were
131   symmetrical, each with a duct area of 0.4 m × 0.4 m and length of 0.8 m. The square ducts were
132   connected to a nozzle or diffuser that was 0.4 m long and had a diameter of 0.23 m at the other
133   end. The nozzle and diffuser were then linked by a 0.6 m-long round pipe as the test section.
134   The purification module, as shown in Fig. 1, was inserted in the middle of the round pipe. All
135   the connections were well sealed to prevent air leakage. At the end of the wind tunnel in the
136   downstream region, a centrifugal fan was installed to extract air through the tunnel. The air
137   velocity in the round duct section could be controlled at 0 to 5 m/s. The rotation speed of the
138   disk could also be controlled by adjusting the electrical voltage.
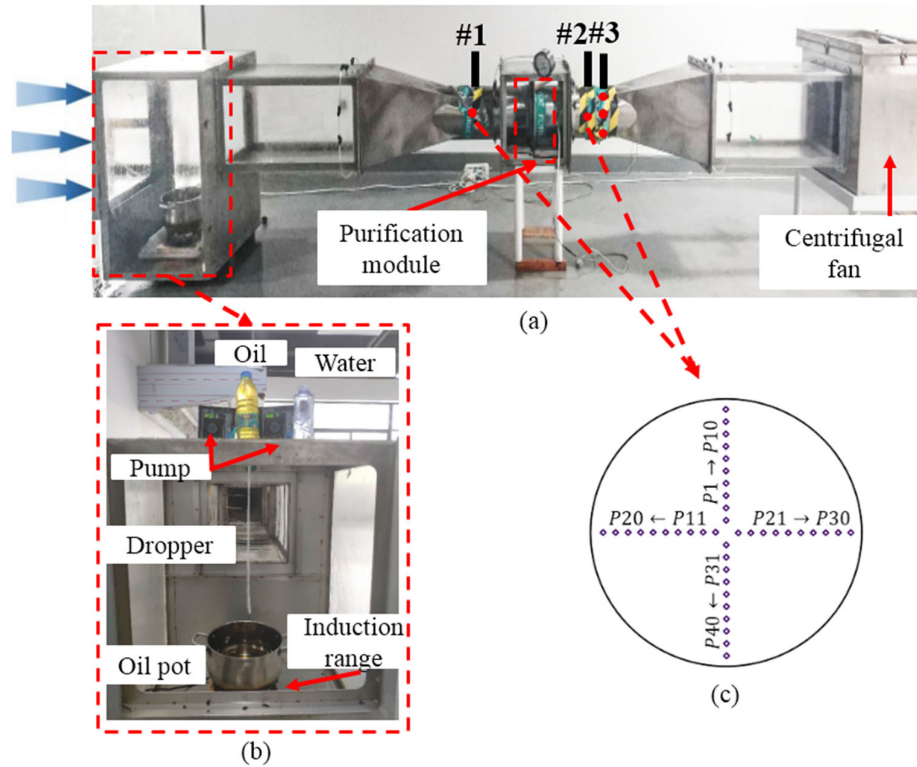
139
140

Fig. 2. (a) Wind tunnel test rig for the rotating disk. (b) Oil particle generator. (c) Velocity
measurement points at Sections #1 and #2.

145   An oil droplet generator was placed in the upstream section of the wind tunnel as shown
146   in Fig. 2 (b). Oil droplets were generated with the use of a peristaltic pump connected to a bottle
147   of water. The pump caused water to drip continuously into a stainless-steel pot filled with corn
148   oil at a temperature between 270 and 280°C. The oil temperature was monitored by an infrared
149   thermal camera. The water flow rate was 0.025 ml/s. The stainless-steel pot was 25 cm in
150   diameter and 14 cm in depth, and it was heated by an induction range with adjustable heating
151   power. The pot initially contained 800 ml oil, and a second peristaltic pump connected to a
152   bottle of oil was used to continually refill the pot and maintain a constant oil volume. The oil
153   drip rate was 0.076 ml/s. Table 1 lists the technical specifications of the instruments used in the
154   experiment.

155
156

Table 1. Instrument specifications

Type of instrument	Model	Range and accuracy

Aerosol spectrometer	Palas Promo 3000	0.2 to 105 μm; 1 to 10^6 p/cm^3
Thermal image	Fluke 520tix	-20 to 850°C (± 2 K)
Anemometer	TSI 9545	0 to 50 m/s (± 3%)
Voltage regulator	STG-2000W	0 to 300 V (1 V)

157

158   An aerosol spectrometer (Model Promo 3000 from Palas, Germany) was used for
159 measuring particle size distribution and number concentration. The spectrometer had 128 size
160 channels with four measuring ranges. The measurement was based on the light scattering effect
161 and Mie dispersion theory. Since the Sauter diameter of particles were detected, the mass
162 concentration can be calculated by the control unit as

163
$$C_{mi} = \frac{n_i \pi x_i^3 \rho}{6 V_m} \tag{1}$$

164 where C_{mi} represents mass of particles within the size channel i, n_i the measured number of
165 particles within the channel i, x_i arithmetic medium diameter in size channel i, ρ particle
166 diameter, and V_m measuring volume. V_m is defined as

167

168
$$V_m = u \cdot s \cdot t_{meas} \tag{2}$$

169 where u represents particle velocity, s optical cross section area of the sensor and t_{meas}
170 measurement duration. (Koivisto et al. 2012; Song and Hu 2017). The size range in our
171 experiment was from 2 to 105 microns, and the sampling frequency was 1 Hz. As shown in Fig.
172 2, the sampling point was at the center of Section #1, which was in the upstream section at a
173 distance of 0.25 m from the rotating disk. Fig. 3 shows the mean value of mass concentration
174 and size distribution of the oil droplets from eight repeated measurements. The particle
175 generator was stable, generating <8 micron particles with a standard deviation of <0.005, 8-12
176 micron particles with a standard diviation <0.01 and 12–18 micron particles with a standard
177 deviation <0.015. The reason was that particle number larger than 12 micron was lower than
178 1P/cm^3, compared with 2 micron particles at 65P/cm^3. The extreme low concentration made
179 random error higher. In addition, we believe that larger particles were more likely to be affected
180 by the gravitational deposition effect, so the particles larger than 12 micron were excluded. The
181 measured particles had a peak mass concentration at 6.5 microns. This study selected particles
182 in the 3–11 micron range for evaluating the capture efficiency of the rotating disk.
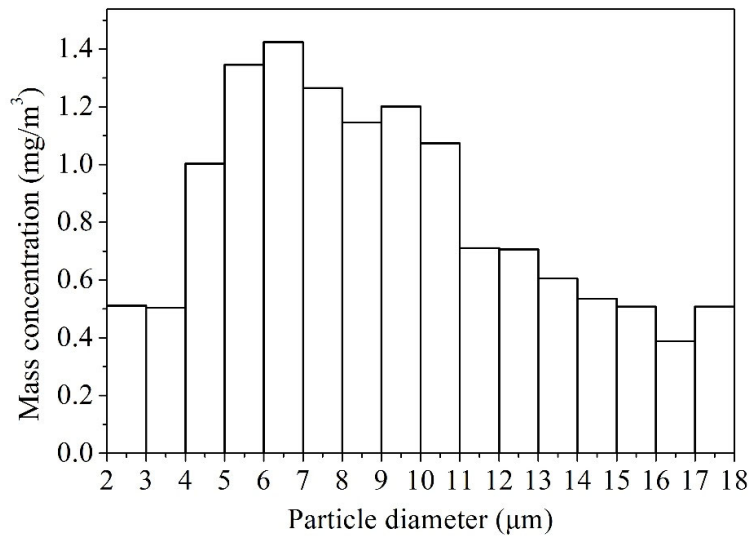
183

184

Fig. 3. Mean value of mass concentration and size distribution of the oil droplets from eight repeated measurements.

According to Chinese standard GB/T 17713-2011, the recommended minimum airflow rate for kitchen exhaust hoods is 600 m³/h. Meanwhile, IEC 2011 recommends a minimum airflow rate of 420 m³/h based on the odor reduction factor (Chen et al. 2018). Our research studied exhaust rates of 320, 450 and 600 m³/h, taking into account the significant fumes generated by Chinese cooking. The corresponding air velocities through the round pipe section were 2.16, 3.02 and 4.00 m/s, respectively, measured at Section #1. Since the rotating disk can influence the airflow distribution in the downstream region, the air velocity was also measured at Section #2, which was 0.25 m downstream from the disk. A hot-wire anemometer (Model 9545 from TSI, USA) was used for the air velocity measurements. There were a total of 40 measurement points for air velocity in each section, as shown in Fig. 2. (c). Since the air velocity fluctuated significantly, it was measured for 10 min at each point with a measuring frequency of 1 Hz. All the data along each radius was averaged to obtain the area-averaged velocity. Disk rotation speeds of 800, 1500 and 2050 rpm were investigated.

The particle concentrations were measured at three different positions in Section #3, which was 0.35 m downstream from the disk. The measurement took 8 min at each position. The capture efficiency, *CE*, of the rotating disk was determined by

$$CE = 1 - \frac{C_{on}}{C_{off}} \tag{3}$$

where C_{on} represents the particle mass concentrations when the disk rotated at a specific speed, and C_{off} the particle mass concentrations when the disk did not rotate.

2.2 CFD model

CFD can predict turbulent flows by direct numerical simulation (DNS), large-eddy simulation (LES), and Reynolds-averaged Navier-Stokes (RANS) equation simulation with turbulence models (Ansys 2013). DNS resolves the whole spectrum of turbulent scales without any modeling, making it unfeasible for flow through a rotating disk because the required grid number would be too high and the computing time too long. Whereas small eddies are modeled, in LES large eddies are resolved directly Resolving only the large eddies allows the use of much coarser mesh and larger time steps in LES than in DNS. However, LES still requires significantly finer meshes than those customarily used for RANS calculations. As a result, the computational cost associated with LES is normally one or two orders of magnitude higher than that for steady RANS calculations in terms of computer memory and CPU time (Zhai et al. 2007). Therefore, LES was not affordable for this project.

RANS equations govern the transport of the averaged flow quantities over the whole range of the scales of turbulence being modeled. RANS equation modeling thus greatly reduces the required computational effort and resources, and was therefore selected for this study. In accordance with the modeling approach for Reynolds stresses, RANS turbulence models are further divided into eddy-viscosity models and Reynolds-stress models.

Eddy-viscosity models employ the Boussinesq hypothesis to relate the Reynolds stresses to the mean velocity gradients:

$$-\rho \overline{u_i' u_j'} = \mu_t (\frac{\partial u_i}{\partial x_j} + \frac{\partial u_j}{\partial x_i}) - \frac{2}{3}(\rho k + u_t \frac{\partial u_k}{\partial x_k})\delta_{ij} \tag{4}$$

231 The most popular eddy-viscosity models are the k-ε models. The advantage of this approach is
232 the comparatively low cost associated with the computation of the turbulent viscosity, μ_t. In the
233 case of the k-ε models, two additional transport equations (for turbulence kinetic energy, k, and
234 turbulence dissipation rate, ε) are solved.(Ansys, 2013) The μ_t is computed by combining k and
235 ε as follows:

236
$$\mu_t = \rho C_\mu \frac{k^2}{\varepsilon} \tag{5}$$

237
238 where C_μ is a constant. The disadvantage of the Boussinesq hypothesis as presented is that it
239 assumes that μ_t is isotropic, which may not be true for our study. In contrast, Reynolds stress
240 models do not use the isotropic eddy-viscosity hypothesis; they close the RANS equations by
241 solving transport equations for the Reynolds stresses, together with an equation for the
242 dissipation rate. Thus, seven additional transport equations are solved for three-dimensional
243 flows. This study compared simulations using Reynold stress model (Gibson and Launder
244 1978), the standard k- ε model (Launder and Spalding 1983) and re-normalization group (RNG)
245 k- ε model (Yakhot and Orszag 1986) for the flow through the rotating disk. Note that not all
246 the turbulent models should be tested. For example, Realizable k-ε model would produce non-
247 physical turbulent viscosities and unreliable results when the computational domain contains
248 rotating and stationary fluid zones(Ansys 2013). The content of rotating and stationary fluid
249 will be discussed later. With the corresponding experimental data. The best model could then
250 be identified for further study.
251   This investigation used the Gambit 2.4.6 software program (GAMBIT 2, 2005) to create
252 the mesh for the disk geometry. Since the diameter of the wires was very thin at 0.28 mm, the
253 mesh had very fine grid distribution around the wires and a large grid number. By considering
254 the periodic nature of the disk wires and supporting bar geometrically, this study created a mesh
255 model for one eighth of the disk and then used periodic boundary conditions to construct the
256 whole purification module, as shown in Fig. 4 (a). A grid-independence study with 3.42, 5.86
257 and 8.60 million-cell grids found that the simulation should use at least 5.86 million tetrahedral
258 cells. The grid-independence test was shown in Fig 4 (b). Fig. 4 (c) shows the grid around the
259 wires, and the cell skewness was below 0.85. The mesh surrounding the wires and the
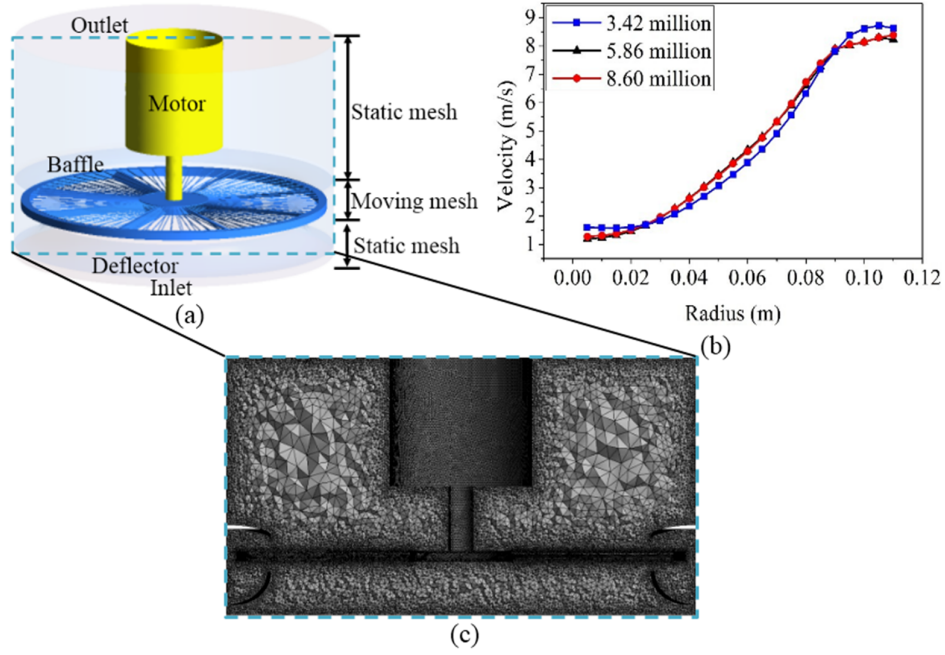260 supporting bar was very fine because of the high velocity gradients in these regions.
261

262
263 *Fig. 4. (a) Purification module used for simulations. (b) Grid-independence test. (c) Grid*
264 *distribution of the vertical section in the module.*
265
266   To simulate the rotating disk, this study used the multiple reference frame model and the
267 sliding mesh method (Ansys, 2013). The multiple reference frame model is a simple steady-
268 state calculation method that reduces computational expense. The sliding mesh method was
269 then used to solve the flow field as well as particle distribution since this method can deliver a
270 truly time-dependent solution (Ashraf Ali et al. 2013). The multiple reference frame model used
271 a rotating frame for the region containing the wires and support bar, while a stationary frame
272 was applied to the nonmoving part as shown in Fig. 4. (a). The flow in the rotating region was
273 solved using the rotating framework, and the results served as the boundary conditions for the
274 stationary region. At the same time, the solution from the stationary region was used as the
275 boundary conditions for the rotating region. In a similar manner to that of the multiple reference
276 frame model, the sliding mesh method divided the geometry into a rotating part and a stationary
277 part. However, the mesh in the rotating region physically moved during the transient solution.
278 After each time step, i.e., after each motion of the rotating mesh, the RANS and the mass
279 continuity equations were solved iteratively (Appa et al. 2013; Hörmann et al. 2011).
280   This investigation used a coupled algorithm to solve the pressure-velocity coupling, which
281 can accelerate convergence; the PRESTO! scheme to discretize the pressure, considering the
282 problem of swirl flow with a high-pressure gradient; and the second-order upwind scheme to
283 discretize the momentum equation. The inlet to the purification module was set as the velocity
284 inlet, and the outlet as the pressure outlet. The numerical solving process was iterative until a
285 converged solution was obtained. After 14,000 iterations, the mass continuity residual was
286 lower than 1% of the mass flow rate through the rotating disk.
287   This study used the Eulerian–Lagrangian approach for solving particle motion with one-
288 way coupling, which means that the particle phase had no impact on the airflow. Particles were
289 injected into the flow domain through the inlet as shown in Fig. 5. Particle-to-particle
290 interactions were neglected because the volume fraction of particles was low. When the
291 particles entered the flow, their trajectories were governed by the particle momentum equation
292 obtained directly from Newton's second law (Zamankhan et al. 2006):
293

294
$$\frac{d\vec{v}_p}{dt} = F_D(\vec{v} - \vec{v}_p) + \frac{g(\rho_p - \rho)}{\rho_p}$$
(6)

295

296 where v is the air velocity, v_P the particle velocity, ρ the fluid density and ρ_P is the density of
297 the particle. The first term on the right side of Eq. (6) represents the drag force, and the second
298 term the buoyancy force. The drag force can be calculated by

299
$$F_D = \frac{18\mu}{\rho_P d_p^2} \frac{C_D \, \text{Re}}{24}$$
(7)

300 where μ is the molecular viscosity of the fluid and d_P is particle diameter. The drag

301 coefficient, C_D, for smooth particles is $C_D = a_1 + \dfrac{a_2}{\text{Re}} + \dfrac{a_3}{\text{Re}^2}$, where a_1, a_2, and a_3 are

302 constants that apply over several ranges of Re given by Morsi and Alexander (1972). Re is the
303 relative Reynolds number, which is defined as

304
$$\text{Re} \equiv \frac{\rho d_p \left| \overrightarrow{v_p} - \vec{v} \right|}{\mu}$$
(8)

305 The discrete random walk model was employed to model the turbulent dispersion of particles
306 by integrating the trajectory equations for individual particles, using the instantaneous fluid
307 velocity, $\overline{u} + u'$, along the particle path during the integration. The fluctuating velocity
308 components are Gaussian distributed random value and are kept constant over an interval of
309 time given by the characteristic lifetime of the eddies. The interaction of a particle with a
310 succession of discrete stylized fluid-phase turbulent eddies was simulated. As soon as a particle
311 hit a solid surface, it was considered trapped because of the high viscidity of oil fumes. The
312 simulations were performed for particle diameters ranging from 3 to 11 microns. The particle
313 emission number was determined by the grid number of the injection surface, which was 3,156.
314 By controlling the emission time, we released 9,468 and 94,680 particles, respectively, and we
315 found that the number of the particles had no effect on the capture efficiency analysis. The
316 capture efficiency was that the number of particles captured by the solid surface over the total
317 number of particles entered the inlet.
318   This investigation calculated the time step size from the minimum mesh size divided by
319 the highest speed of airflow in the domain. The time step size was 0.3 mm (around the wires) /
320 27.4 m/s (around the tip of the wires), which equals 0.011 ms. We compared the results with
321 three different time steps, 0.005, 0.01 and 0.02 ms, and found 0.01 ms to be sufficiently good.
322 Approximately 1,500 steps were needed for the particles to either pass through or be trapped
323 by the disk. A typical simulation took roughly two days of computing time on a workstation
324 with 48 GB memory, a 64 bit operating system, a CPU with 12 cores and 24 threads and a 2.4
325 GHz processor.

326

327 **3. Results**

328

329 **3.1 Validation of the CFD model**

330

331   This investigation obtained nine sets of data on particle capture efficiency from the wind
332 tunnel, for three air velocities and three disk rotation speeds; the data was then used for
333 validating the CFD model. We selected the case with airflow rate of 10 m^3/min (or 4.0 m/s
334 mean axial air velocity), which corresponds to one of the common flow rates of hoods on the
335 market. The rotation speed of the disk was 2,050 rpm. Fig. 5. (a) shows the air velocity profiles
336 measured at Section #2. The data reveals an asymmetrical velocity profile, which was due to
337 the slight asymmetry of the disk installation in the wind tunnel. The results show that the greater

the distance from the center in the radial direction, the higher the air velocity was. As displayed in red circle, the data was averaged for comparison with the CFD results in Fig. 5 (b).

Because of the complex flow feature studied, this investigation used three popular turbulence models to simulate the airflow and compared the results. As shown in Fig. 5. (b), the RNG k-ε model performed very poorly in predicting the air velocity distribution in the core region. The standard k- ε and RSM models yielded very similar results that were in reasonable agreement with the experimental data, although the RSM model seemed to perform slightly better. The RSM model provided the most accurate prediction within a radius of 0.07 m. In the far outer annular region, without experimental data, the RSM model would predict better air velocity if the experimental data could be extrapolated. Therefore, this study used the RSM model for further investigation.
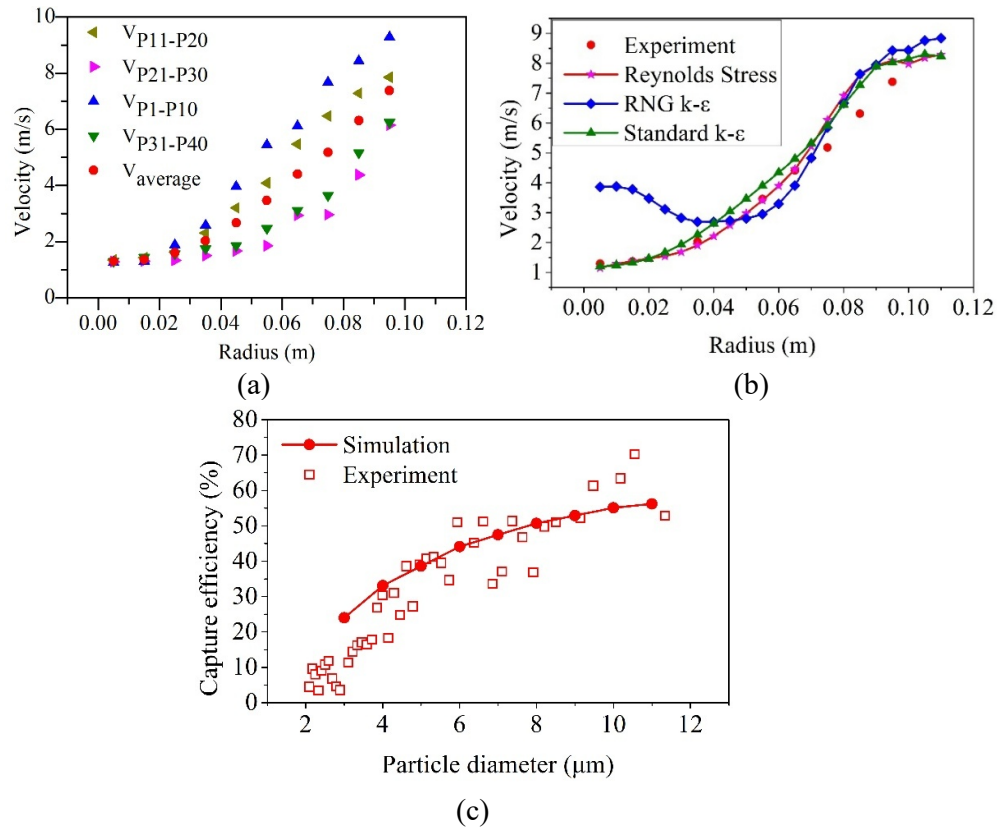

(a)

(b)

(c)

Fig. 5. (a) Velocity measured in the wind tunnel at Section #2. (b) Comparison of the air velocity profiles predicted by the three turbulence models with the experimental data at Section #2. (c) Comparison of experimental and simulated capture efficiency versus particle diameter

Fig. 6(a) shows the velocity distribution calculated by CFD at Section #2. As with the measured data, the air velocity was lowest in the core region and increased with the radius. In the annular region, the air velocity was not uniform along the tangential direction, because of the supporting bar. By averaging the air velocity in the tangential direction, we obtained the radial, tangential, and axial air velocity components, as depicted in Fig. 6(b). The radial velocity was generally small, while the tangential velocity increased with the radius. As a result of the swirl effect, the flow in the core region was reversed, and thus the axial velocity was negative. In the annular region, where the flow was moving downstream, the axial velocity was positive.
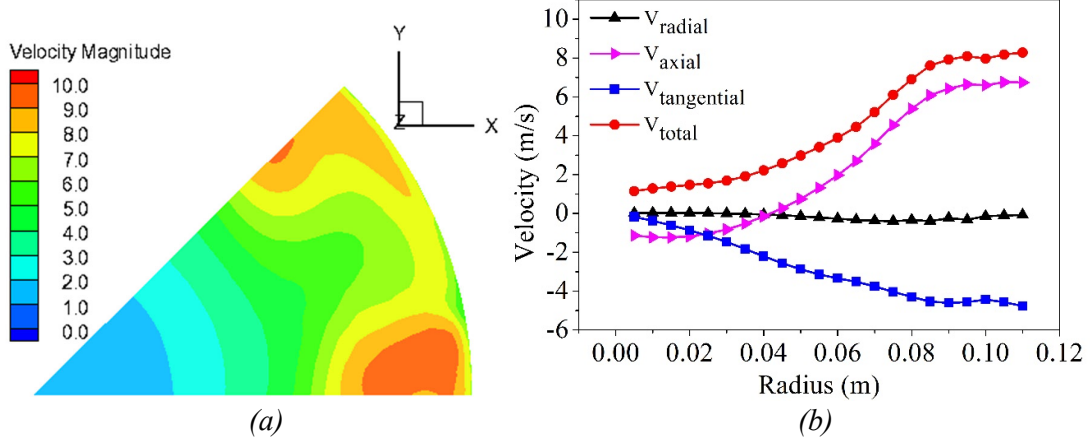
367
368 *(a)* *(b)*
369
370 *Fig. 6. (a) Computed air velocity distribution at Section #2 in the downstream region and (b)*
371 *computed air velocity components in the radial direction.*
372
373   Fig. 5. (c) compares the simulated capture efficiency with the measured data for different
374 particle sizes. For larger sizes, the difference between the simulated and measured capture
375 efficiency was higher. Many factors could have contributed to the discrepancy. For example,
376 asymmetry in installation of the disk could lead to experimental error. The CFD simulations
377 used many approximations that could also have contributed to the discrepancy. When large
378 particles passed the rotating disk, the high-speed swirl effect could have caused them to collide
379 with each other and coagulate to larger particles, and thus the capture efficiency in the
380 experiment could exceed the simulated one. In contrast, small particles were less likely to
381 coagulate.
382   The above comparison between the CFD results and experimental data confirmed that
383 CFD with the RSM model could predict the air velocity distribution and particle capture
384 efficiency in the test rig with acceptable accuracy. Therefore, we considered the CFD model
385 validated, and it was used for further analysis in this investigation.
386
387 **3.2 Mechanism of particle capture by a rotating disk**
388
389 There are three basic mechanisms that lead to the capture of particles in a rotating disk
390 medium. These are interception, inertial impaction, and Brownian diffusion. Brownian
391 diffusion is only important for small particles (about 200 nm or less). Interception is
392 important when the size of the particle and disk diameter are comparable. Inertial impaction
393 becomes considerable when the particle's momentum is not negligible. Within the size range
394 of the particles analyzed, only inertial impaction (Rubenstein and Koehl 1977) was
395 considered. Particles tended to follow the streamlines until the fluid was diverted and
396 accelerated as it passed around the moving wires. Because of their own inertia, the particles
397 would then deviate from the streamlines and collide with the wires. The deposition intensity
398 by inertial impact for a static filter (Fuchs and Davies 1964) can be written as:

399 $$N_I = \frac{(\rho_p - \rho_m)d_p^{\,2}V_o}{18\mu d_f} \qquad\qquad (5)$$

400 where ρ_p is the density of particles, ρ_m fluid density, V_o air velocity, d_f the diameter of the wires
401 and d_p particle diameter. The equation indicates that a small increase in particle diameter would
402 lead to a large increase in the intensity of inertial impaction.

403   In order to better understand the mechanism of particle capture by a rotating disk, this
404   study used the validated CFD model to calculate particle trajectories through the disk. Fig. 7
405   shows the trajectories calculated for particles with different diameters (5, 10, 15, and 20 μm).
406   The particles were injected at eight positions that were equally spaced along the radius on the
407   inlet surface, namely, from r = 0.02 to 0.09 m, as shown in Fig. 7. (a). The results illustrate the
408   difficulty of capture by the wires when the particles were small. The capture efficiency
409   increased with the particle size. As shown in Fig. 7. (b) to (e), the number of particles captured
410   by the wires of different diameters was 1, 4, 5, and 8, respectively. The results indicate that
411   particles with a diameter of 20 μm or larger would be completely captured. Particles that have
412   passed through the disk would rotate and move towards the outside layer because of the
413   centrifugal force effect. The initial particle trajectory at r = 0.02 m was quite different from the
414   others, since the area around the motor was under negative pressure. In addition, the particle
415   injected at r = 0.09 m moved faster than the others, since the deflector accelerated its speed.
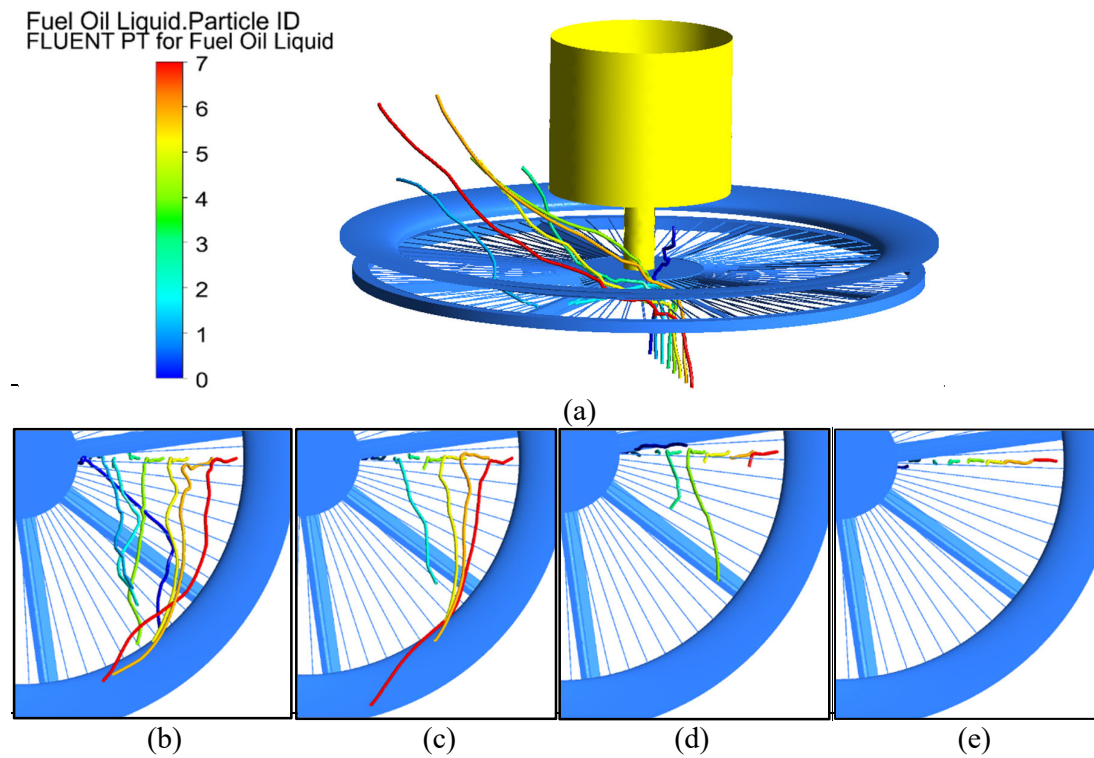416

417
418   (a)

419
420   (b)   (c)   (d)   (e)
421   *Fig. 7. Trajectories of particles with different diameters: (a) 3D view (b) 5 μm (c) 10 μm (d)*
422   *15 μm and (e) 20 μm.*
423

3.3 Influencing parameters for capture efficiency
424
425

426   This investigation also studied key parameters that could influence capture efficiency,
427   such as disk rotation speed, airflow velocity, and disk structure. The results are discussed below.
428   The rotation speed can significantly affect the capture efficiency of the disk. Fig. 8. (a)
429   compares the computed and measured capture efficiency at three different rotation speeds (800,
430   1500, 2050 rpm) when the air velocity was 4.00 m/s. Particles with diameters of 5 μm and 10
431   μm were selected for this study. The results show that the capture efficiency increased with the
432   rotation speed. When the rotation speed increased from 800 rpm to 2,050 rpm, the capture
433   efficiency increased by 23.6% in the simulation and 19.3% in the experiment for 10 μm
434   particles. The reason for the increase is that with a higher rotation speed, the wires swept a
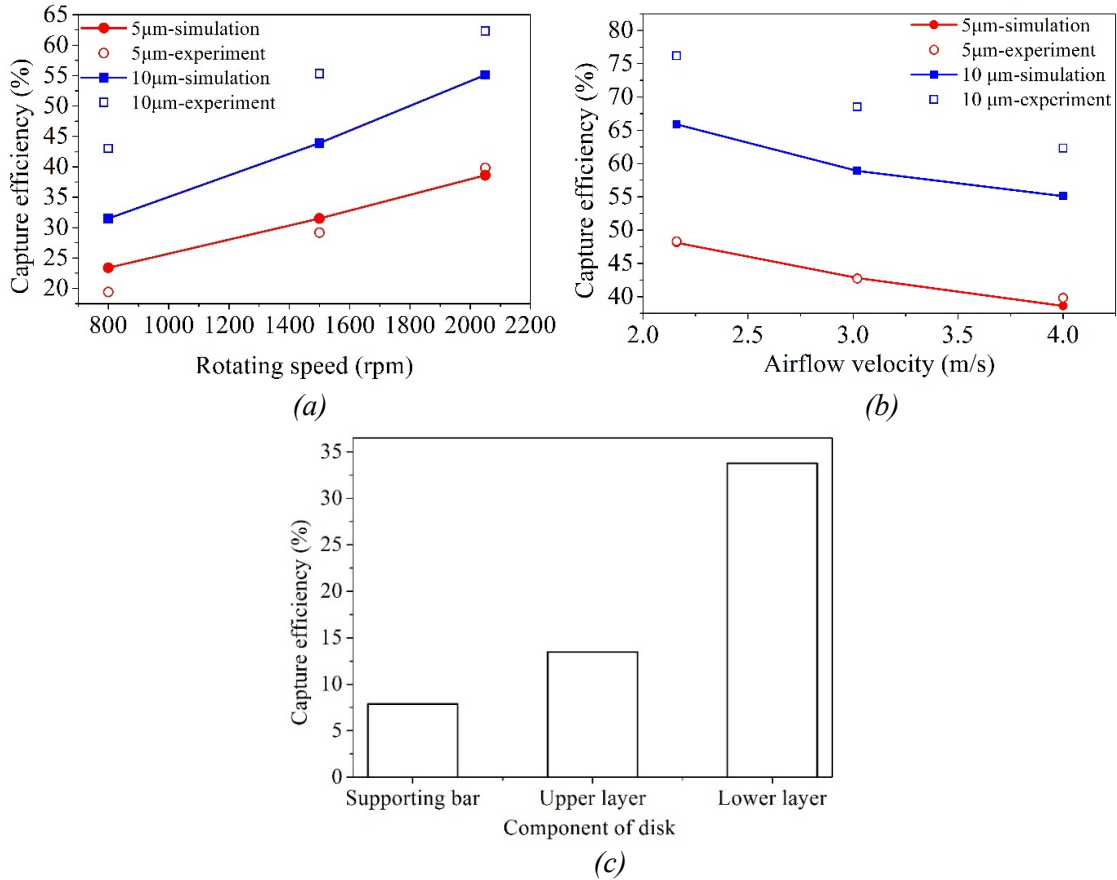435   greater area per unit of time and were more likely to collide with particles.

(a) *(b)*

(c)

Fig. 8. Particle capture efficiency vs. (a) disk rotation speeds when the airflow velocity was 4.00 m/s. (b) airflow velocity when the disk rotated at 2,050 r/min. (c) disk components.

Fig. 8 (b) displays the capture efficiency of the rotating disk at different flow velocities (2.16, 3.02, and 4.00 m/s). The capture efficiency increased when the air velocity decreased. At a low air velocity, particles entrained in the flow moved slowly in the axial direction, which allowed more contact time with the wires and thus a higher possibility of capture. When the air velocity decreased from 4 m/s to 2.16 m/s, the capture efficiency increased by around 10% for the two particle sizes. The results from both Fig. 8 (a) and (b) show good agreement between the computed and measured capture efficiency for the 5 micron particle but not for the 10 micron particles.

Next, this study used the CFD results to quantify the capture of particles by different parts of the rotating disk. Figure 8 (c) displays the efficiency of capture by different parts for 10 μm particles. The results indicate that the supporting bar, upper-layer wires and lower-layer wires caught 7.9% 13.5% and 33.8% of the particles, respectively. The lower-layer wires caught more particles than the upper-layer wires because there was a higher concentration of particles in the lower air region. The supporting bar had a small area that was concentrically distributed. The bar was not intentionally designed for capturing particles.

4   Improvement methods

Taking into account the capture mechanism and parameter analysis, we proposed several ways to enhance the performance of the rotating disk design. One idea for enhancing the disk

467 performance was to increase the possibility of collision between particles and the wires. The
468 first method was to use a larger number of wires. Although the wires were twined densely near
469 the center of the disk, the wires in the outer region were relatively sparse. Adding more wires
470 in this region can increase the likelihood of collision. We divided the wire zone into three
471 sections as shown in Fig. 9. (a), doubling the number of wires in the middle zone and
472 quadrupling the number in the outer zone. At a 2,050 rpm rotation speed and 4 m/s air velocity,
473 and with the use of 10 μm particles in our CFD simulations, the capture efficiency would
474 increase from 55.1% in the original disk to 75.9% if more wires were added to the lower layer,
475 as shown in Table 3. Meanwhile, the pressure drop through the disk would also increase
476 moderately, from 54.0 Pa in the original disk to 66.1 Pa. If more wires were added to both layers
477 of the disk, the capture efficiency and pressure drop would further increase, as illustrated in
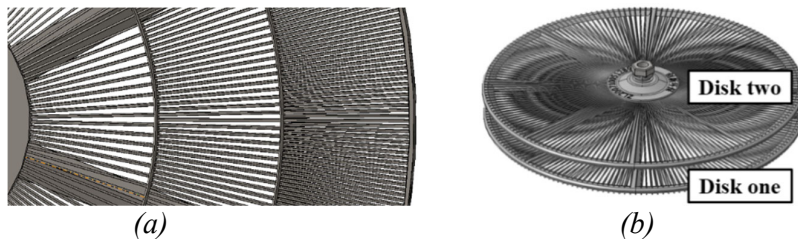478 Table 3. The approach seems to be advantageous.
479

480
481 *(a)* *(b)*
482 *Fig. 9. Improvement methods: (a) adding more wires and (b) using a double disk*
483
484 *Table 2. Improvement in capture efficiency by adding more wires to the rotating disk*

	Capture efficiency	Pressure drop (Pa)
Original disk	55.1%	54.0
Denser lower layer only	75.9%	66.1
Two denser layers	79.1%	74.0
Two disks rotating in same direction	71.1%	90.4
Two disks rotating in opposite directions	84.1%	100.0

485
486   The second method was the addition of another rotating disk above the original one, as
487 shown in Fig. 9 (b). Two disks rotating in the same direction and in opposite directions,
488 respectively, were simulated. Table 2 shows that the capture efficiency would increase from
489 55.1% for the original disk to 71.1% if two disks rotated in the same direction. However, the
490 pressure drop through the disks would increase from 54.0 Pa in the original disk to 90.4 Pa. If
491 two disks rotated in opposite directions, the capture efficiency would increase further to 84.1%,
492 and the pressure drop would rise to 100.0 pa. The reason for this greater increase was that when
493 the two disks rotated in opposite directions, compared with rotation in the same direction, the
494 relative velocity of the particles and the wires of the upper disk ("Disk two" in Fig. 9 (b)) would
495 increase as particles passed through the upper disk. This would enhance the possibility of
496 collision between particles and wires. The method of two disks rotating in opposite directions
497 achieved 5% higher capture efficiency than two denser layers, but it resulted in a much higher
498 pressure drop. As the flagship device of cyclonic filter from Jeven company and Halton
499 company, the capture efficiency arrives at 90% at the cost of 120 pa pressure drop or even
500 higher (Natalia 2012), which proved that our improvements of rotating disk effective and
501 practical.
502

5 Conclusions

This investigation used experimental measurements and CFD simulations to study the capture efficiency of a rotating disk in a kitchen hood. The study led to the following conclusions:

Among the three turbulence models tested, the Reynolds stress model yielded the best agreement with the measured air velocity distribution in a duct with the rotating disk. The agreement in predicting capture efficiency was better for small particles than for large particles. The standard k-ε model may also be used, whereas the RNG k-ε model did not perform well for the complex flow.

The results indicate that larger particles were more likely to be captured because of their greater inertial effect and higher likelihood of colliding with the disk wires. The capture efficiency increased with rotation speed but decreased with increasing airflow rate. The lower layer of wires was more capable of capturing particles than the upper layer because of higher particle concentration in the lower-layer region.

This investigation proposed two methods to improve the disk design. Adding more wires to the middle and outer regions of a rotating disk would increase the capture efficiency with a moderate increase in pressure drop through the disk. The addition of a second disk above the original one, to form a double-disk system, would increase the capture efficiency with a higher pressure drop through the disk.

References

Alexander, G.D., Salpietra, J.A., 2012. Grease removal apparatus, systems and methods. Google Patents.

Ansys (2013a). Ansys Fluent 15.0 theory Guide. Ansys Inc.

Ansys (2013a). Ansys Fluent 15.0 User's Guide. Ansys Inc.

Antoun, G.S., 1999. Cyclonic filter assembly. Google Patents.

Appa, H., Deglon, D.A., Meyer, C.J., 2013. Numerical modelling of hydrodynamics and gas dispersion in an autoclave. Hydrometallurgy. 131-132, 67-75.

ASHRAE Standard 62.1, 2007. Ventilation for acceptable indoor air quality, American society of heating, refrigerating, and air conditioning engineers, Atlanta.

Ashraf, Ali. B., Janiga, G., Temmel, E., Seidel-Morgenstern, A., Thévenin, D. 2013. Numerical analysis of hydrodynamics and crystal motion in a batch crystallizer. Journal of Crystal Growth. 372, 219-229.

Chen, W., Li, J., Wang, C., Dai, X., Liu, J., 2018. 2D-PIV measurement of range hood-driven flow in a domestic kitchen. Energy and Buildings. 177, 64-76.

Delp, W.W., Singer, B.C., 2012. Performance assessment of U.S. residential cooking exhaust hoods. Environ Sci Technol. 46, 6167-73.

Fuchs, N., Davies, C.J.S., 1964. Aerosol Mechanics.(Book Reviews: The Mechanics of Aerosols). 146, 1033-1034.

GAMBIT 2, 2005. User's Manual to GAMBIT 2. Fluent Inc.

552   Gao, J., Cao, C., Xiao, Q., Xu, B., Zhou, X., Zhang, X., 2013. Determination of dynamic intake
553   fraction of cooking-generated particles in the kitchen. Building and Environment. 65,
554   146-153.
555   GBT 17713-2011 range hood, 2011.
556   Gibson, M., Launder, B., 1978. Ground effects on pressure fluctuations in the atmospheric
557   boundary layer. Journal of scientific computing. 86, 491-511.
558   Hörmann, T., Suzzi, D., Khinast, J.G., 2011. Mixing and Dissolution Processes of
559   Pharmaceutical Bulk Materials in Stirred Tanks: Experimental and Numerical
560   Investigations. Industrial & Engineering Chemistry Research. 50, 12011-12025.
561   Huber, K.L., 2005. Cyclonic air filter with exit baffle. Google Patents.
562   Kang, K., Kim, H., Kim, D.D., Lee, Y.G., Kim, T., 2019. Characteristics of cooking-generated
563   PM10 and PM2. 5 in residential buildings with different cooking and ventilation types.
564   Science of the Total Environment. 668, 56-66.
565   Koivisto, A.J., Yu, M., Hämeri, K., Seipenbusch, M., 2012. Size resolved particle emission
566   rates from an evolving indoor aerosol system. Journal of Aerosol Science. 47, 58-69.
567   Kwok, K.C., Robison, R., 2011. Impact filter with grease trap. Google Patents.
568   Launder, B.E., Spalding, D.B., 1983. The numerical computation of turbulent flows. Numerical
569   prediction of flow, heat transfer, turbulence and combustion. Elsevier. pp. 96-116.
570   Li, C.S., Lin, W.H., Jenq, F., 1993. Size distributions of submicrometer aerosols from cooking.
571   Environment International. 19, 147-154.
572   Li, W., Li, S., Gao, J., Cao, Y., Chen, Y., 2017. Grease separation in cooking fume by using a
573   dynamic rotary filter, Chinese Journal of Environmental Engineering. 11, 2926-32.
574   Lu, F., Shen, B., Yuan, P., Li, S., Sun, Y., Mei, X., 2019. The emission of PM2. 5 in respiratory
575   zone from Chinese family cooking and its health effect. Science of the Total
576   Environment. 654, 671-677.
577   Lunden, M.M., Delp, W.W., Singer, B.C., 2015. Capture efficiency of cooking-related fine and
578   ultrafine particles by residential exhaust hoods. Indoor Air. 25, 45-58.
579   Metayer, C., Wang, Z., Kleinerman, R.A., Wang, L., Brenner, A.V., Cui, H., et al., 2002.
580   Cooking oil fumes and risk of lung cancer in women in rural Gansu, China. Lung
581   Cancer. 35, 111-117.
582   Natalia, S., 2012. Problem of grease and its solutions in commercial kitchens. Mikkeli
583   University of applied Sciences.
584   POPE, III. C., 2000. What do epidemiologic findings tell us about health effects of
585   environmental aerosols? Journal of Aerosol Medicine. 13, 335-354.
586   Rajendran, N., Otzen, K.G., 1990. Baffle type hood and duct filters for commerical use. Google
587   Patents.
588   Rim, D., Wallace, L., Nabinger, S., Persily, A., 2012. Reduction of exposure to ultrafine
589   particles by kitchen exhaust hoods: the effects of exhaust flow rates, particle size, and
590   burner position. Sci Total Environ. 432, 350-6.
591   Rubenstein, D.I., Koehl, M.A.R., 1977. The mechanisms of filter feeding: some theoretical
592   considerations. The American Naturalist. 111, 981-994.
593   See, S.W., Balasubramanian, R., 2006. Risk assessment of exposure to indoor aerosols
594   associated with Chinese cooking. Environmental Research. 102, 197-204.
595   See, S.W., Balasubramanian, R., 2006. Physical characteristics of ultrafine particles emitted
596   from different gas cooking methods. 6, 82-92.
597   See, S.W., Balasubramanian, R., 2008. Chemical characteristics of fine particles emitted from
598   different gas cooking methods. Aerosol and Air Quality Research. 42, 8852-8862.
599   Singer, B.C., Delp, W.W., Price, P.N., Apte, M.G., 2012. Performance of installed cooking
600   exhaust devices. Indoor Air. 22, 224-34.

601   Song, J., Hu, X., 2017. A mathematical model to calculate the separation efficiency of
602   streamlined plate gas-liquid separator. Separation and Purification Technology. 178,
603   242-252.
604   Sun, D., 2009. Research on Purification of Dynamic Net-disk Purifier and Design of Control
605   System. Wu Han University of Technology.
606   Sze-To, G.N., Wu, C.L., Chao, C.Y., Wan, M.P., Chan, T.C., 2012. Exposure and cancer risk
607   toward cooking-generated ultrafine and coarse particles in Hong Kong homes.
608   HVAC&R Research. 18, 204-216.
609   Torkmahalleh, M.A., Goldasteh, I., Zhao, Y., Udochu, N.M., Rossner, A., Hopke, P.K., et al.,
610   2012. PM2.5 and ultrafine particles emitted during heating of commercial cooking oils.
611   Indoor Air. 22, 483-91.
612   Wang, L., Xiang, Z., Stevanovic, S., Ristovski, Z., Salimi, F., Gao, J., et al., 2017. Role of
613   Chinese cooking emissions on ambient air quality and human health. Science of the
614   Total Environment. 589, 173-181.
615   Welch, A., Kuehn, T., 2003. Development of a draft method of test for determining grease
616   removal efficiencies, American society of heating, refrigerating, and air conditioning
617   engineers, final report, ASHRAE 1151-RP.
618   Xiao, D., Deng, S., Zhang, J., Liu, B., Yuan, D., 2018. Effects of cooking oil fume on ambient
619   air quality, Chinese Journal of Environmental Engineering. 36, 434-445.
620   Yakhot, V., Orszag, S.A., 1986. Renormalization group analysis of turbulence. I. Basic theory.
621   Journal of scientific computing. 1, 3-51.
622   Zamankhan, P., Ahmadi, G., Wang, Z., Hopke, P.K., Cheng, Y.S., Su, W.C., et al., 2006.
623   Airflow and Deposition of Nano-Particles in a Human Nasal Cavity. Aerosol Science
624   and Technology. 40, 463-476.
625   Zhai, Z.J., Zhang, Z., Zhang, W., Chen, Q.Y., 2007. Evaluation of Various Turbulence Models
626   in Predicting Airflow and Turbulence in Enclosed Environments by CFD: Part 1—
627   Summary of Prevalent Turbulence Models. HVAC&R Research. 13, 853-870.
628   Zhu, C., Li, M., Miao, Y., Fan, N., Li, J., 2014. Analysis of characters of particulate
629   emissions generated from urban cooking fume. Green Building. 5, 57-61.
630